

1 **Technical note: 12-km resolution capability for the global GEOS-Chem model of atmospheric**
2 **composition**

3 Xiaolin Wang¹, Melissa P. Sulprizio¹, Yuyao Zhuge², Randall V. Martin², Daniel J. Jacob¹

4 ¹ School of Engineering and Applied Sciences, Harvard University, Cambridge, MA, USA

5 ² Department of Energy, Environmental & Chemical Engineering, Washington University in St.
6 Louis, St. Louis, MO, USA

7

8 *Correspondence to:* Xiaolin Wang (wangxi@g.harvard.edu)

9

10

11 **Abstract**

12

13 We present a new 12-km nested resolution capability in the GEOS-Chem global model of
14 atmospheric composition. This capability can be applied to simulations for any user-selected
15 domain worldwide from March 2021 onward by accessing a new hourly cubed-sphere C720
16 (approximately 12 km × 12 km resolution) global wind archive from the NASA GEOS-FP
17 meteorological data assimilation system. We regridded the archive to support rectilinear GEOS-
18 Chem Classic nested grid simulations worldwide at 0.125° × 0.15625° resolution and denote this
19 as the 12-km GEOS-Chem capability. We evaluate this 12-km configuration of GEOS-Chem by
20 comparison with the standard 25-km (0.25° × 0.3125° resolution) nested configuration in
21 simulations of transport tracers, oxidant-aerosol chemistry, and inversions of satellite data using
22 the Integrated Methane Inversion (IMI). The 12-km simulation features stronger vertical
23 transport (up to 20% lower surface ²²²Rn concentrations) because it better captures horizontal
24 convergence both spatially and temporally. Aerosol lifetimes against deposition are shorter by a
25 few percent. The 12-km oxidant-aerosol chemistry can better simulate urban observations of
26 NO₂, and shows stronger ozone urban titration together with slightly higher surface ozone
27 background due to enhanced vertical transport. 12-km and 25-km inversions using the IMI show
28 highly consistent results on the regional scale, but the 12-km inversion provides greater
29 information and improved spatial detail to resolve emissions from different sectors.

30

31 **1. Introduction**

32 GEOS-Chem (<http://geos-chem.org>) is an open-source global 3-D model of atmospheric
33 chemistry originally described by Bey et al. (2001) and used by hundreds of research groups
34 around the world for a wide range of applications. The standard offline configuration of GEOS-
35 Chem is driven by archived Goddard Earth Observing System (GEOS) meteorological data from
36 the NASA Global Modeling and Assimilation Office (GMAO), with no feedback of chemistry on
37 meteorology. GEOS-Chem can also operate online in dynamical coupling with Earth system
38 models (Fritz et al., 2022; Hu et al., 2018; Lu et al., 2020) or the WRF regional model (Lin et al.,

39 2020). Here we introduce the capability to conduct offline GEOS-Chem simulations at $0.125^\circ \times$
40 0.15625° ($\approx 12 \text{ km} \times 12 \text{ km}$) resolution by exploiting a new GEOS advection data archive (grid-
41 scale winds) available from March 2021 onward. This enables low-cost, reproducible, high-
42 resolution simulations of atmospheric chemistry and air quality anywhere in the world through
43 the nested capability of GEOS-Chem. In what follows we refer to it as the 12-km capability in
44 GEOS-Chem.

45 The open-access GEOS global meteorological datasets used to drive GEOS-Chem are produced
46 at GMAO by data assimilation on the cubed-sphere grid of the underlying GEOS Earth system
47 model (ESM) and then archived on a rectilinear latitude-longitude grid for public dissemination.
48 The GEOS-Chem Support Team extracts from these archives the data needed to run GEOS-
49 Chem and distributes them to users as an open dataset library through the Amazon Web Services
50 (AWS) cloud (Zhuang et al., 2019; Martin et al., 2022). GEOS-Chem users may choose from
51 three main datasets: the Modern-Era Retrospective Analysis for Research and Applications,
52 version 2 (MERRA-2; 1980-present) at $0.5^\circ \times 0.625^\circ$ resolution, the GEOS Forward Processing
53 (GEOS-FP; 2014-present) at $0.25^\circ \times 0.3125^\circ$ resolution, and the GEOS for Instrument Teams
54 (GEOS-IT; 1998-present) at $0.5^\circ \times 0.625^\circ$ or native cubed-sphere C180 resolution (180 grid cells
55 per cubed-sphere side, approximately $50 \text{ km} \times 50 \text{ km}$ resolution). MERRA-2 provides a long
56 stable record with fixed physics and data assimilation algorithms, GEOS-IT is the next-
57 generation stable record with updated physics and data assimilation, and GEOS-FP is the
58 operational product generated in near real time using the latest validated GEOS system. GEOS-
59 FP operates at native C720 resolution (approximately $12 \text{ km} \times 12 \text{ km}$) but the data archive was
60 previously made available only at $0.25^\circ \times 0.3125^\circ$ resolution. Since March 2021, GMAO has been
61 producing a native-resolution hourly C720 GEOS-FP advection archive specifically to serve
62 GEOS-Chem needs, and this is what we use to enable the 12-km capability in GEOS-Chem.

63 GEOS-Chem operates in two modes, Classic (GC-Classic) and High-Performance (GCHP)
64 (Martin et al., 2022). GC-Classic is designed for easy use on the rectilinear longitude-latitude
65 grid and operates on single-node mode with shared-memory parallelization. GCHP enables high-
66 resolution simulations using distributed-memory parallelization (MPI) on the cubed-sphere grid
67 with efficient multi-node scalability extending to thousands of cores (Eastham et al., 2018). Both
68 GC-Classic and GCHP can use the original rectilinear GEOS archive available at resolutions
69 down to $0.25^\circ \times 0.3125^\circ$, with GCHP converting these inputs to its cubed-sphere grid at runtime.
70 They can also operate at coarser resolutions for computational economy using regridded GEOS
71 data archived on AWS as part of the GEOS-Chem input dataset library. Global GC-Classic
72 simulations thus typically use $2^\circ \times 2.5^\circ$ or $4^\circ \times 5^\circ$ GEOS data. GC-Classic includes a one-way
73 nested capability to conduct regional simulations over limited domains with archived dynamic
74 boundary conditions from a coarse-resolution simulation (Wang et al., 2004). GCHP includes a
75 stretched-grid capability to enable higher-resolution two-way nesting over target regions (Bindle
76 et al., 2021). Emission and surface type information are generally available at $0.1^\circ \times 0.1^\circ$

77 resolution from the GEOS-Chem input dataset library, from which they are regridded on the fly
78 within GEOS-Chem at the desired resolution using the HEMCO software tool (Lin et al., 2021).
79 The one-way nested GC-Classic capability at GEOS-FP $0.25^\circ \times 0.3125^\circ$ (referred to as 25-km)
80 resolution is widely used for air quality applications (Kim et al., 2015; Zhang et al., 2015) and
81 for inversions of greenhouse gas data to infer surface fluxes (Varon et al., 2022).

82 Here, we implement the GEOS-FP native C720 advection archive for use in GC-Classic nested-
83 grid simulations. This 12-km capability can be applied over any user-selected domain
84 worldwide, and for any period from March 2021 onward. It has been released in GEOS-Chem
85 14.6.0 (<https://doi.org/10.5281/zenodo.15243271>). We describe the 12-km capability in Section 2
86 and compare its transport to the standard 25-km nested GC-Classic configuration in Section 3.
87 We then demonstrate its application to a full-chemistry simulation over the North China Plain
88 (Section 4) and to the inversion of satellite observations using the Integrated Methane Inversion
89 (IMI) framework (Section 5).

90 **2. GEOS-Chem simulation at 12-km resolution**

91 GC-Classic allows users to conduct nested simulations over any domain of interest using the
92 GEOS meteorological archives as input and with rectilinear coordinates specified at runtime.
93 This framework was first introduced by Wang et al. (2004) and updated to $0.25^\circ \times 0.3125^\circ$
94 resolution by Zhang et al. (2015) and Kim et al. (2015). The nested simulations are conducted as
95 a regional model with boundary conditions provided by a separate global simulation at $2^\circ \times 2.5^\circ$
96 or $4^\circ \times 5^\circ$ resolution that provides dynamic chemical fields updated every three hours.

97 Here we use the new global C720 GEOS-FP hourly advection archive, regridded to $0.125^\circ \times$
98 0.15625° , to produce the 12-km advection archive that enables GC-Classic nested-grid
99 simulations at $0.125^\circ \times 0.15625^\circ$ resolution. The 12-km advection archive includes horizontal
100 wind vectors, surface pressure, and specific humidity on 72 vertical levels extending from the
101 surface to 0.01 hPa (model top). Horizontal wind vectors are converted from cubed-sphere C720
102 mass flux data for use in the GC-Classic transport scheme (Lin and Rood, 1996). Surface
103 pressure is needed to infer the vertical air mass fluxes from the horizontal air mass fluxes by
104 mass conservation. Specific humidity is needed to convert wet air fluxes and pressure in the
105 GEOS data to dry air fluxes and pressures used in GEOS-Chem. The regridding from cubed-
106 sphere C720 to the rectilinear $0.125^\circ \times 0.15625^\circ$ grid yields an approximately $12 \text{ km} \times 12 \text{ km}$
107 horizontal scale over midlatitudes, slightly coarser toward the equator and finer toward the poles.

108 Table 1 summarizes the GEOS-FP input data for the 12-km configuration as compared to the 25-
109 km configuration. The idea behind the advection archive is that higher resolution is most needed
110 for the winds to better represent eddy flows and to leverage the $0.1^\circ \times 0.1^\circ$ resolution of the
111 emission data. Limiting the number of variables in the advection archive enables global data
112 storage at C720. The 12-km advection archive has hourly temporal resolution, compared to 3-

113 hourly resolution for the 3-D variables in the 25-km archive. Other non-advection meteorological
 114 inputs including convective mass fluxes and vertical mixing depths are from the standard GEOS-
 115 FP archive at $0.25^\circ \times 0.3125^\circ$ resolution and are dynamically regridded to $0.125^\circ \times 0.15625^\circ$ at
 116 runtime. Most emission datasets are available on a $0.1^\circ \times 0.1^\circ$ grid and are regridded at runtime to
 117 the simulation resolution using HEMCO (Lin et al., 2021). The 12-km archive is available
 118 globally. We also maintain separate 12-km advection archives for five continental regions
 119 (Africa, Asia, Europe, North America, and South America) to reduce data size and thereby speed
 120 up data access and processing over the user-selected nested domains
 121 (<https://registry.opendata.aws/geoschem-nested-input-data>; latest access: 21 October 2025).

122 All simulations presented here were carried out on the Harvard Cannon v2.0 supercomputing
 123 cluster using compute nodes equipped with dual-socket Intel Xeon Platinum 8480CL CPUs (56
 124 cores each, base frequency ~ 2.9 GHz). Each simulation used 48 physical CPU cores and ran on a
 125 single node. We find that the 12-km simulation wall-time is about 7 times that of a 25-km
 126 simulation over the same domain. This is driven by the 4 times increase in grid cells and the 2
 127 times reduction in timestep. The 1-month full-chemistry simulation presented in Section 4 took
 128 26 wall-time hours to complete at 12-km resolution.

129

130 **Table 1.** GEOS-FP meteorological data archives available for driving GEOS-Chem at $0.125^\circ \times$
 131 0.15625° (12-km) and $0.25^\circ \times 0.3125^\circ$ (25-km) resolutions^a.

GEOS-Chem simulation	12-km	25-km
Archive period	March 2021-present	January 2014-present
Horizontal resolution (advection)	$0.125^\circ \times 0.15625^\circ$	$0.25^\circ \times 0.3125^\circ$
Temporal resolution (advection)	Hourly	3-hourly
Horizontal resolution (other)	$0.25^\circ \times 0.3125^\circ$ regridded to $0.125^\circ \times 0.15625^\circ$	$0.25^\circ \times 0.3125^\circ$
Temporal resolution (other)	3-hourly or hourly ^b	3-hourly or hourly
Timestep ^c	Transport 150 s Non-transport 300 s	Transport 300 s Non-transport 600 s

132 a. For GC-Classic simulations at $0.125^\circ \times 0.15625^\circ$ and $0.25^\circ \times 0.3125^\circ$ resolutions with 72
 133 hybrid sigma-pressure vertical levels extending up to 0.01 hPa. GEOS-FP meteorological
 134 data used as GEOS-Chem input include advection variables (horizontal wind vectors,
 135 surface pressure, specific humidity) and other variables driving convective transport,
 136 planetary boundary layer (PBL) mixing, emissions, radiation, chemistry, and deposition.
 137 The full list of variables is at: <https://wiki.seas.harvard.edu/geos->

138 chem/index.php/List_of_GEOS-FP_met_fields. The advection variables are grouped in a
139 separate advection archive for 12-km applications. The 12-km and 25-km archives are
140 available globally, and also for individual continents to speed up data extraction.
141 b. Hourly for two-dimensional fields such as surface properties and PBL depth; 3-hourly for
142 three-dimensional fields such as temperature and convective mass flux.
143 c. Recommended timesteps for operator splitting (Philip et al., 2016), can be adjusted by
144 user. Non-transport operators include emissions, chemistry, and deposition.

145

146 3. Transport tracer simulations

147 We use the TransportTracers simulation of GEOS-Chem (Zhang et al., 2021) to evaluate model
148 transport and scavenging processes. This simulation includes 21 generic species (tracers) to test
149 the different components of GEOS-Chem transport. We focus here on the radionuclide tracers
150 radon-222 (^{222}Rn), lead-210 (^{210}Pb), and beryllium-7 (^7Be), which are routinely used to
151 benchmark transport and wet deposition in GEOS-Chem (Liu et al., 2001; Yu et al., 2018). These
152 tracers are particularly useful for evaluating model vertical transport, whereas grid-scale vertical
153 winds are calculated from horizontal mass flux convergence and is not directly available in the
154 model. The nested-grid simulations are conducted over eastern China (100–125°E, 17–45°N,
155 domain shown in Figure 1) at both $0.125^\circ \times 0.15625^\circ$ and $0.25^\circ \times 0.3125^\circ$ resolutions for February
156 and June 2022. Initial conditions are generated from spin-up simulations at the same resolutions,
157 starting from October 2021 (corresponding to spin-up periods of 4 months for February and 8
158 months for June). The boundary conditions are updated every three hours from a global
159 simulation at $2^\circ \times 2.5^\circ$ resolution.

160 Figure 1 shows surface ^{222}Rn concentrations from the 12-km simulation and relative differences
161 with the 25-km simulation. ^{222}Rn in the simulation has a spatially uniform soil source and is
162 removed by radioactive decay with a half-life of 3.8 days, making it a sensitive tracer for vertical
163 transport in the troposphere (Liu et al., 2001; Yu et al., 2018). Surface ^{222}Rn concentrations are
164 lower by 0–20% at 12-km than at 25-km resolution. Differences are most pronounced over
165 complex terrain such as Sichuan and Taiwan. The total ^{222}Rn burden in the two simulations is the
166 same, and the difference is in the vertical distribution (Figures 2 and 3). The 12-km simulation
167 shows lower ^{222}Rn concentrations in the lower troposphere and higher concentrations in the
168 middle-to-upper troposphere, indicating stronger vertical transport. The lower ^{222}Rn
169 concentrations in the tropical stratosphere in June, combined with the lower ^7Be concentrations
170 below the tropopause, may reflect greater restriction of transport across the tropopause at higher
171 resolution (Stanevich et al., 2020) but would require further investigation because the absolute
172 changes are very small.

173 Transport processes in GEOS-Chem include grid-resolved advection (winds), sub-grid
174 parameterized convection (convective mass fluxes), and PBL-mixing (Lin and McElroy, 2010).
175 Differences between the 12-km and 25-km simulations could reflect stronger vertical winds at
176 12-km due to better resolved horizontal convergence (Yu et al., 2018) and better resolution of
177 concentration gradients leading to stronger tracer convergence for the same winds. To separate
178 these two effects, we conducted a 12-km sensitivity simulation driven by the 3-hourly 25-km
179 advection archive regridded to 12-km resolution during runtime (right columns of Figures 1-3).
180 We find that both effects contribute.

181 ^{210}Pb (half-life of 22.3 years) is produced by the decay of ^{222}Rn , and ^7Be (half-life of 53.3 days)
182 is generated by cosmic-ray interactions with atmospheric oxygen and nitrogen at high altitudes.
183 Both radionuclides rapidly attach to aerosol particles and are subsequently transported and
184 removed by wet and dry deposition. This makes ^{210}Pb useful to evaluate aerosol transport and
185 removal processes, with ^7Be providing complementary information on stratosphere–troposphere
186 exchange and tropospheric subsidence (Liu et al., 2001). Comparisons of 12-km and 25-km
187 simulations for ^{210}Pb show similar differences as for ^{222}Rn (Figures 2 and 3) but weaker in
188 magnitude because the ^{210}Pb source is more diffuse. Lifetimes against deposition differ by less
189 than 2% between the 12-km and 25-km simulations. Comparisons for ^7Be also show weaker
190 differences than for ^{222}Rn because vertical transport of ^7Be in the troposphere is mainly by large-
191 scale subsidence, which is less sensitive to eddy motions. The ^7Be lifetime against deposition is
192 3% higher at 25-km resolution, explaining the slightly higher overall tropospheric
193 concentrations.

194

195 **4. Full-chemistry simulations**

196 We perform 1-month full-chemistry simulations for February and June of 2022 over the North
197 China Plain (NCP; domain shown in Figure 4) at 12-km and 25-km horizontal resolutions for
198 comparison. The full-chemistry configuration of GEOS-Chem includes detailed ozone– NO_x –
199 VOCs–aerosol– halogen tropospheric and stratospheric chemistry (Wang et al., 2021). Boundary
200 conditions are provided by a global $2^\circ \times 2.5^\circ$ GEOS-Chem simulation and updated every three
201 hours, and spin-up simulations are conducted from October 2021 to generate initial conditions.
202 Monthly anthropogenic emissions are from the MIXv2 Asian emission inventory at $0.1^\circ \times 0.1^\circ$
203 resolution for 2017, scaled to 2022 using province-level emission data from the MEIC v1.4
204 inventory (Zheng et al., 2018) and mapped to the 12-km and 25-km grids using HEMCO. We
205 compare the model simulations of surface NO_2 , ozone, and fine particulate matter ($\text{PM}_{2.5}$)
206 concentrations to hourly observations from 361 sites operated by the China National
207 Environmental Monitoring Centre (CNEMC; <http://www.cnemc.cn>, last assess: 23 May 2023).
208 The sites are mainly urban. We remove anomalous observations at each site following the quality

209 control protocols described in Lu et al. (2018). We sample model outputs at the observation sites
210 for comparisons.

211 Figure 4 shows the afternoon (13-18 local time) surface NO_2 concentrations over the NCP in
212 June 2022 and the effect of model resolution. The finer structure at 12-km resolution is evident
213 and largely reflects the ability to exploit the higher resolution of emissions. Comparison to
214 CNEMC observations (Figure 5a) shows a low bias in the model, likely reflecting the near-
215 source locations of the sites, but the bias is reduced at 12-km resolution. The 12-km simulation
216 does not improve the correlation with observations for individual CNEMC sites, which could
217 reflect errors in model transport or in the spatial distribution of emissions.

218 Figure 6 compares simulated maximum daily 8-h average (MDA8) surface ozone concentrations
219 at 12-km and 25-km resolutions in June 2022. The differences between the two resolutions are
220 generally smaller than 5 ppb, and there is no significant difference in the fit to observations
221 (Figure 5b). Background ozone concentrations increase by up to 3 ppb over the northern NCP
222 region, likely driven by increased vertical transport of ozone from aloft as seen in the simulated
223 ^7Be concentrations in Figure 1. Increasing the model resolution to 12-km decreases surface
224 ozone concentrations by about 3 ppb in Beijing and 6 ppb in Tianjin city core areas, as expected
225 from higher NO_x concentrations driving stronger ozone titration, whereas suburban areas exhibit
226 ozone increases of no more than 2 ppb. These effects are too small to be effectively evaluated in
227 the comparison to observations (Figure 5b).

228 Figure 7 shows the daily-averaged total $\text{PM}_{2.5}$ mass concentrations in February 2022, where
229 $\text{PM}_{2.5}$ is computed in the model as the sum of fine aerosol components (Zhai et al., 2021). We
230 focus on February here because $\text{PM}_{2.5}$ concentrations are higher in winter than in summer (Zhai
231 et al., 2019). $\text{PM}_{2.5}$ concentrations are in general slightly lower at 12-km resolution because of
232 the enhanced vertical transport. However, higher concentrations are found in a few urban
233 hotspots due to primary organic aerosol emissions from combustion that are better resolved
234 spatially. Again, differences are too small to be arbitrated by the observations (Figure 5c).

235

236 **5. Application to the Integrated Methane Inversion (IMI)**

237 The IMI applies the nested GEOS-Chem as forward model in regional analytical inversions of
238 TROPOMI satellite observations of methane columns to optimize methane emissions (Estrada et
239 al., 2025; Varon et al., 2022). It uses Bayesian inference to minimize the mismatch between the
240 TROPOMI methane column observations and the corresponding concentrations simulated by
241 GEOS-Chem, regularized by prior information on emissions. GEOS-Chem is applied to
242 construct the Jacobian matrix describing the sensitivity of TROPOMI observations to emissions
243 as simulated by the model transport. This is then used together with the TROPOMI observations,
244 prior emission estimates, and prior and observational error statistics to derive optimized
245 (posterior) emissions. The TROPOMI satellite observations are at $5.5 \times 7 \text{ km}^2$ pixel resolution so

246 there is potential benefit for conducting the inversion at 12-km resolution using our new GEOS-
247 Chem capability. The 12-km IMI configuration was previously applied in Wang et al. (2026) to
248 quantify methane emissions across 12 U.S. urban areas. Here we examine how inversion results
249 vary between 12-km and 25-km resolution, focusing on the Houston urban area in eastern Texas
250 as an example.

251 The IMI inversion procedure is described by Estrada et al. (2025) and Hancock et al. (2025),
252 including the design of state vector, error estimates, and optimization strategy. Here we optimize
253 annual methane emissions in 2022 over a $3^\circ \times 4^\circ$ (latitude \times longitude) domain encompassing
254 Houston and its surrounding area as shown in Figure 8. The state vector to be optimized consists
255 of emissions in each land-containing grid cell of the $3^\circ \times 4^\circ$ domain (496 elements at 12-km
256 resolution and 164 elements at 25-km resolution) and boundary conditions on each lateral edge
257 (4 elements). Our prior estimates of anthropogenic emissions are from the U.S. Environmental
258 Protection Agency Greenhouse Gas Inventory (GHGI) at $0.1^\circ \times 0.1^\circ$ resolution for 2020
259 (Maasackers et al., 2023). Natural emissions follow the default configuration as described in
260 Estrada et al. (2025). We assume a lognormal prior error probability density function (PDF) for
261 emissions with a geometric error standard deviation of 2.0 (Bruno et al., 2025), and a normal
262 error PDF for boundary conditions with a 10 ppb error standard deviation. The IMI analytical
263 inversion returns posterior emissions and a posterior error covariance matrix from which the
264 averaging kernel matrix can be derived as a measure of information content from the
265 observations (Brasseur and Jacob, 2017).

266 The prior estimate of total emissions over the $3^\circ \times 4^\circ$ inversion domain is 790 Gg a^{-1} (Figure 8).
267 Total posterior emissions are 50% higher than the prior estimate and agree closely between the
268 12-km inversion (1260 Gg a^{-1}) and the 25-km inversion (1170 Gg a^{-1}). The 12-km inversion
269 results, when averaged over the 25-km grid, show a high degree of consistency with the 25-km
270 inversion results over the inversion domain (spatial correlation coefficient = 0.92). The trace of
271 the averaging kernel matrix defines the Degrees of Information for Signal (DOFS) indicating the
272 number of pieces of information that can be obtained from the observations through the inversion
273 independently from the prior estimate. The DOFS for the $3^\circ \times 4^\circ$ domain is 24.4 for the 12-km
274 inversion, higher than the 16.8 for the 25-km inversion. Conducting the inversion at higher
275 resolution allows for more information on emissions to be extracted from the observations.

276 Another advantage of the higher-resolution inversion is better separation of the sectors
277 contributing to methane emissions. Sectoral information in the inversion is obtained by
278 attributing the posterior/prior emission ratios for each grid cell to the different sectors
279 contributing emissions to that grid cell in the prior estimate (Wecht et al., 2014). Higher spatial
280 resolution in the inversion reduces spatial overlap between sectors.

281 **6. Conclusion**

282 We have implemented a 12-km resolution nested capability in the GEOS-Chem global model of
283 atmospheric chemistry by taking advantage of a new hourly GEOS advection archive available
284 globally from March 2021 onward and freely distributed to GEOS-Chem users through the AWS
285 cloud. We compared the 12-km simulation to the standard 25-km nested simulation in GEOS-
286 Chem for transport tracers (^{222}Rn , ^{210}Pb , ^7Be), ozone-aerosol chemistry, and inversion of methane
287 satellite data where GEOS-Chem provides the forward model. The 12-km simulation has
288 stronger vertical transport (up to 20% decrease in ^{222}Rn surface concentrations) because of
289 improved representation of horizontal convergence. It shows finer spatial structure in surface
290 pollutants (NO_2), with improved capability to reproduce urban observations. It better represents
291 surface ozone titration in urban air and slightly increases the surface ozone background by
292 increasing vertical transport. Application to the Integrated Methane Inversion (IMI) shows
293 regional-scale results consistent with a 25-km inversion but higher information content and
294 greater spatial detail. Overall, this 12-km capability further extends the application of GEOS-
295 Chem in regional atmospheric chemistry and in the use of high-resolution satellite observations
296 to quantify emissions of air pollutants and greenhouse gases at fine spatial scales. Higher model
297 resolution improves the representation of finer concentration gradients and inverse model
298 sensitivity through improved transport and chemistry.

299

300 **Code and data availability.**

301 The source code of GEOS-Chem 14.6.0 is publicly available at
302 <https://doi.org/10.5281/zenodo.15243271>. The GEOS-FP meteorological fields used to drive
303 GEOS-Chem are available on the Amazon Web Services (AWS) cloud
304 (<https://s3.amazonaws.com/gcgrid/index.html>; last access: 21 October 2025).

305

306 **Author contributions.**

307 XW and DJJ conceptualized the research. XW performed the analyses and data visualization.
308 XW and MPS developed the model code. MPS, YZ and RVM contributed to the data collection.
309 XW and DJJ wrote the manuscript with input from all authors.

310

311 **Competing interests.**

312 The authors declare no competing interests.

313

314 **Financial support.** This research has been supported by the United Nations Environment
315 Programme's International Methane Emissions Observatory (IMEO) and by the NASA
316 Atmospheric Composition Modeling and Analysis Program (grant no. 80NSSC23K0926). RVM
317 acknowledges support from the U.S. National Science Foundation (NSF; grant no. 2244984).

318

319 **References**

320 Bey, I., Jacob, D. J., Yantosca, R. M., Logan, J. A., Field, B. D., Fiore, A. M., Li, Q., Liu, H. Y.,
321 Mickley, L. J., and Schultz, M. G.: Global modeling of tropospheric chemistry with assimilated
322 meteorology: Model description and evaluation, *J. Geophys. Res. Atmospheres*, 106, 23073–
323 23095, <https://doi.org/10.1029/2001JD000807>, 2001.

324 Bindle, L., Martin, R. V., Cooper, M. J., Lundgren, E. W., Eastham, S. D., Auer, B. M., Clune, T.
325 L., Weng, H., Lin, J., Murray, L. T., Meng, J., Keller, C. A., Putman, W. M., Pawson, S., and
326 Jacob, D. J.: Grid-stretching capability for the GEOS-Chem 13.0.0 atmospheric chemistry
327 model, *Geosci. Model Dev.*, 14, 5977–5997, <https://doi.org/10.5194/gmd-14-5977-2021>, 2021.

328 Brasseur, G. P. and Jacob, D. J.: *Modeling of Atmospheric Chemistry*, 1st ed., Cambridge
329 University Press, <https://doi.org/10.1017/9781316544754>, 2017.

330 Bruno, J. H., Jacob, D. J., Wang, X., Sulprizio, M. P., Estrada, L. A., Varon, D. J., Wofsy, S. C.,
331 Omara, M., and Gautam, R.: Integrating MethaneAIR aircraft and TROPOMI satellite

332 observations in the Integrated Methane Inversion (IMI) to optimize methane emissions,
333 EGU sphere, 1–23, <https://doi.org/10.5194/egusphere-2025-4626>, 2025.

334 Eastham, S. D., Long, M. S., Keller, C. A., Lundgren, E., Yantosca, R. M., Zhuang, J., Li, C.,
335 Lee, C. J., Yannetti, M., Auer, B. M., Clune, T. L., Kouatchou, J., Putman, W. M., Thompson, M.
336 A., Trayanov, A. L., Molod, A. M., Martin, R. V., and Jacob, D. J.: GEOS-Chem High
337 Performance (GCHP v11-02c): a next-generation implementation of the GEOS-Chem chemical
338 transport model for massively parallel applications, *Geosci. Model Dev.*, 11, 2941–2953,
339 <https://doi.org/10.5194/gmd-11-2941-2018>, 2018.

340 Estrada, L. A., Varon, D. J., Sulprizio, M., Nesser, H., Chen, Z., Balasus, N., Hancock, S. E., He,
341 M., East, J. D., Mooring, T. A., Oort Alonso, A., Maasakkers, J. D., Aben, I., Baray, S., Bowman,
342 K. W., Worden, J. R., Cardoso-Saldaña, F. J., Reidy, E., and Jacob, D. J.: Integrated Methane
343 Inversion (IMI) 2.0: an improved research and stakeholder tool for monitoring total methane
344 emissions with high resolution worldwide using TROPOMI satellite observations, *Geosci. Model*
345 *Dev.*, 18, 3311–3330, <https://doi.org/10.5194/gmd-18-3311-2025>, 2025.

346 Fritz, T. M., Eastham, S. D., Emmons, L. K., Lin, H., Lundgren, E. W., Goldhaber, S., Barrett, S.
347 R. H., and Jacob, D. J.: Implementation and evaluation of the GEOS-Chem chemistry module
348 version 13.1.2 within the Community Earth System Model v2.1, *Geosci. Model Dev.*, 15, 8669–
349 8704, <https://doi.org/10.5194/gmd-15-8669-2022>, 2022.

350 Hancock, S. E., Jacob, D. J., Chen, Z., Nesser, H., Davitt, A., Varon, D. J., Sulprizio, M. P.,
351 Balasus, N., Estrada, L. A., Cazorla, M., Dawidowski, L., Diez, S., East, J. D., Penn, E., Randles,
352 C. A., Worden, J., Aben, I., Parker, R. J., and Maasakkers, J. D.: Satellite quantification of
353 methane emissions from South American countries: a high-resolution inversion of TROPOMI
354 and GOSAT observations, *Atmospheric Chem. Phys.*, 25, 797–817, [https://doi.org/10.5194/acp-](https://doi.org/10.5194/acp-25-797-2025)
355 [25-797-2025](https://doi.org/10.5194/acp-25-797-2025), 2025.

356 Hu, L., Keller, C. A., Long, M. S., Sherwen, T., Auer, B., Da Silva, A., Nielsen, J. E., Pawson, S.,
357 Thompson, M. A., Trayanov, A. L., Travis, K. R., Grange, S. K., Evans, M. J., and Jacob, D. J.:
358 Global simulation of tropospheric chemistry at 12.5km resolution: performance and evaluation of
359 the GEOS-Chem chemical module (v10-1) within the NASA GEOS Earth system model (GEOS-
360 5 ESM), *Geosci. Model Dev.*, 11, 4603–4620, <https://doi.org/10.5194/gmd-11-4603-2018>, 2018.

361 Kim, P. S., Jacob, D. J., Fisher, J. A., Travis, K., Yu, K., Zhu, L., Yantosca, R. M., Sulprizio, M.
362 P., Jimenez, J. L., Campuzano-Jost, P., Froyd, K. D., Liao, J., Hair, J. W., Fenn, M. A., Butler, C.
363 F., Wagner, N. L., Gordon, T. D., Welti, A., Wennberg, P. O., Crounse, J. D., St. Clair, J. M.,
364 Teng, A. P., Millet, D. B., Schwarz, J. P., Markovic, M. Z., and Perring, A. E.: Sources,
365 seasonality, and trends of southeast US aerosol: an integrated analysis of surface, aircraft, and
366 satellite observations with the GEOS-Chem chemical transport model, *Atmospheric Chem.*
367 *Phys.*, 15, 10411–10433, <https://doi.org/10.5194/acp-15-10411-2015>, 2015.

368 Lin, H., Feng, X., Fu, T.-M., Tian, H., Ma, Y., Zhang, L., Jacob, D. J., Yantosca, R. M., Sulprizio,
369 M. P., Lundgren, E. W., Zhuang, J., Zhang, Q., Lu, X., Zhang, L., Shen, L., Guo, J., Eastham, S.
370 D., and Keller, C. A.: WRF-GC (v1.0): online coupling of WRF (v3.9.1.1) and GEOS-Chem

371 (v12.2.1) for regional atmospheric chemistry modeling – Part 1: Description of the one-way
372 model, *Geosci. Model Dev.*, 13, 3241–3265, <https://doi.org/10.5194/gmd-13-3241-2020>, 2020.

373 Lin, H., Jacob, D. J., Lundgren, E. W., Sulprizio, M. P., Keller, C. A., Fritz, T. M., Eastham, S.
374 D., Emmons, L. K., Campbell, P. C., Baker, B., Saylor, R. D., and Montuoro, R.: Harmonized
375 Emissions Component (HEMCO) 3.0 as a versatile emissions component for atmospheric
376 models: application in the GEOS-Chem, NASA GEOS, WRF-GC, CESM2, NOAA GEFS-
377 Aerosol, and NOAA UFS models, *Geosci. Model Dev.*, 14, 5487–5506,
378 <https://doi.org/10.5194/gmd-14-5487-2021>, 2021.

379 Lin, J.-T. and McElroy, M. B.: Impacts of boundary layer mixing on pollutant vertical profiles in
380 the lower troposphere: Implications to satellite remote sensing, *Atmos. Environ.*, 44, 1726–1739,
381 <https://doi.org/10.1016/j.atmosenv.2010.02.009>, 2010.

382 Lin, S.-J. and Rood, R. B.: Multidimensional flux-form semi-lagrangian transport schemes, *Mon.*
383 *Weather Rev.*, 124, 2046–2070, [https://doi.org/10.1175/1520-0493\(1996\)124%3C2046:MFFSLT%3E2.0.CO;2](https://doi.org/10.1175/1520-0493(1996)124%3C2046:MFFSLT%3E2.0.CO;2), 1996.

385 Liu, H., Jacob, D. J., Bey, I., and Yantosca, R. M.: Constraints from 210Pb and 7Be on wet
386 deposition and transport in a global three-dimensional chemical tracer model driven by
387 assimilated meteorological fields, *J. Geophys. Res. Atmospheres*, 106, 12109–12128,
388 <https://doi.org/10.1029/2000JD900839>, 2001.

389 Lu, X., Hong, J., Zhang, L., Cooper, O. R., Schultz, M. G., Xu, X., Wang, T., Gao, M., Zhao, Y.,
390 and Zhang, Y.: Severe surface ozone pollution in china: A global perspective, *Environ. Sci.*
391 *Technol. Lett.*, 5, 487–494, <https://doi.org/10.1021/acs.estlett.8b00366>, 2018.

392 Lu, X., Zhang, L., Wu, T., Long, M. S., Wang, J., Jacob, D. J., Zhang, F., Zhang, J., Eastham, S.
393 D., Hu, L., Zhu, L., Liu, X., and Wei, M.: Development of the global atmospheric chemistry
394 general circulation model BCC-GEOS-Chem v1.0: model description and evaluation, *Geosci.*
395 *Model Dev.*, 13, 3817–3838, <https://doi.org/10.5194/gmd-13-3817-2020>, 2020.

396 Maasackers, J. D., McDuffie, E. E., Sulprizio, M. P., Chen, C., Schultz, M., Brunelle, L., Thrush,
397 R., Steller, J., Sherry, C., Jacob, D. J., Jeong, S., Irving, B., and Weitz, M.: A gridded inventory
398 of annual 2012–2018 U.S. anthropogenic methane emissions, *Environ. Sci. Technol.*, 57, 16276–
399 16288, <https://doi.org/10.1021/acs.est.3c05138>, 2023.

400 Martin, R. V., Eastham, S. D., Bindle, L., Lundgren, E. W., Clune, T. L., Keller, C. A., Downs,
401 W., Zhang, D., Lucchesi, R. A., Sulprizio, M. P., Yantosca, R. M., Li, Y., Estrada, L., Putman, W.
402 M., Auer, B. M., Trayanov, A. L., Pawson, S., and Jacob, D. J.: Improved advection, resolution,
403 performance, and community access in the new generation (version 13) of the high-performance
404 GEOS-Chem global atmospheric chemistry model (GCHP), *Geosci. Model Dev.*, 15, 8731–8748,
405 <https://doi.org/10.5194/gmd-15-8731-2022>, 2022.

406 Philip, S., Martin, R. V., and Keller, C. A.: Sensitivity of chemistry-transport model simulations
407 to the duration of chemical and transport operators: a case study with GEOS-Chem v10-01,
408 *Geosci. Model Dev.*, 9, 1683–1695, <https://doi.org/10.5194/gmd-9-1683-2016>, 2016.

409 Stanevich, I., Jones, D. B. A., Strong, K., Parker, R. J., Boesch, H., Wunch, D., Notholt, J., Petri,
410 C., Warneke, T., Sussmann, R., Schneider, M., Hase, F., Kivi, R., Deutscher, N. M., Velazco, V.
411 A., Walker, K. A., and Deng, F.: Characterizing model errors in chemical transport modeling of
412 methane: impact of model resolution in versions v9-02 of GEOS-Chem and v35j of its adjoint
413 model, *Geosci. Model Dev.*, 13, 3839–3862, <https://doi.org/10.5194/gmd-13-3839-2020>, 2020.

414 US Census Bureau, TIGER/Line Shapefile, 2017, 2010 nation, U.S., 2010 Census Urban Area
415 National. [https://catalog.data.gov/dataset/tiger-line-shapefile-2017-2010-nation-u-s-2010-census-](https://catalog.data.gov/dataset/tiger-line-shapefile-2017-2010-nation-u-s-2010-census-urban-area-national)
416 [urban-area-national](https://catalog.data.gov/dataset/tiger-line-shapefile-2017-2010-nation-u-s-2010-census-urban-area-national). Deposited 1 August 2019.

417 Varon, D. J., Jacob, D. J., Sulprizio, M., Estrada, L. A., Downs, W. B., Shen, L., Hancock, S. E.,
418 Nesser, H., Qu, Z., Penn, E., Chen, Z., Lu, X., Lorente, A., Tewari, A., and Randles, C. A.:
419 Integrated Methane Inversion (IMI 1.0): a user-friendly, cloud-based facility for inferring high-
420 resolution methane emissions from TROPOMI satellite observations, *Geosci. Model Dev.*, 15,
421 5787–5805, <https://doi.org/10.5194/gmd-15-5787-2022>, 2022.

422 Wang, X., Jacob, D. J., Downs, W., Zhai, S., Zhu, L., Shah, V., Holmes, C. D., Sherwen, T.,
423 Alexander, B., Evans, M. J., Eastham, S. D., Neuman, J. A., Veres, P. R., Koenig, T. K.,
424 Volkamer, R., Huey, L. G., Bannan, T. J., Percival, C. J., Lee, B. H., and Thornton, J. A.: Global
425 tropospheric halogen (Cl, Br, I) chemistry and its impact on oxidants, *Atmospheric Chem. Phys.*,
426 21, 13973–13996, <https://doi.org/10.5194/acp-21-13973-2021>, 2021.

427 Wang, X., Jacob, D. J., Nesser, H., Balasus, N., Estrada, L. A., Sulprizio, M. P., Cusworth, D. H.,
428 Scarpelli, T. R., Chen, Z., East, J. D., and Varon, D. J.: Quantifying urban and landfill methane
429 emissions in the United States using TROPOMI satellite data, *Sci. Adv.*, 12, eadz9308,
430 <https://doi.org/10.1126/sciadv.adz9308>, 2026.

431 Wang, Y. X., McElroy, M. B., Jacob, D. J., and Yantosca, R. M.: A nested grid formulation for
432 chemical transport over Asia: Applications to CO, *J. Geophys. Res. Atmospheres*, 109,
433 <https://doi.org/10.1029/2004JD005237>, 2004.

434 Wecht, K. J., Jacob, D. J., Frankenberg, C., Jiang, Z., and Blake, D. R.: Mapping of North
435 American methane emissions with high spatial resolution by inversion of SCIAMACHY satellite
436 data, *J. Geophys. Res. Atmospheres*, 119, 7741–7756, <https://doi.org/10.1002/2014JD021551>,
437 2014.

438 Yu, K., Keller, C. A., Jacob, D. J., Molod, A. M., Eastham, S. D., and Long, M. S.: Errors and
439 improvements in the use of archived meteorological data for chemical transport modeling: an
440 analysis using GEOS-Chem v11-01 driven by GEOS-5 meteorology, *Geosci. Model Dev.*, 11,
441 305–319, <https://doi.org/10.5194/gmd-11-305-2018>, 2018.

442 Zhai, S., Jacob, D. J., Wang, X., Shen, L., Li, K., Zhang, Y., Gui, K., Zhao, T., and Liao, H.: Fine
443 particulate matter (PM_{2.5}) trends in China, 2013–2018: separating contributions from
444 anthropogenic emissions and meteorology, *Atmospheric Chem. Phys.*, 19, 11031–11041,
445 <https://doi.org/10.5194/acp-19-11031-2019>, 2019.

446 Zhai, S., Jacob, D. J., Brewer, J. F., Li, K., Moch, J. M., Kim, J., Lee, S., Lim, H., Lee, H. C.,
447 Kuk, S. K., Park, R. J., Jeong, J. I., Wang, X., Liu, P., Luo, G., Yu, F., Meng, J., Martin, R. V.,

448 Travis, K. R., Hair, J. W., Anderson, B. E., Dibb, J. E., Jimenez, J. L., Campuzano-Jost, P., Nault,
449 B. A., Woo, J.-H., Kim, Y., Zhang, Q., and Liao, H.: Relating geostationary satellite
450 measurements of aerosol optical depth (AOD) over East Asia to fine particulate matter (PM_{2.5}):
451 insights from the KORUS-AQ aircraft campaign and GEOS-Chem model simulations,
452 *Atmospheric Chem. Phys.*, 21, 16775–16791, <https://doi.org/10.5194/acp-21-16775-2021>, 2021.

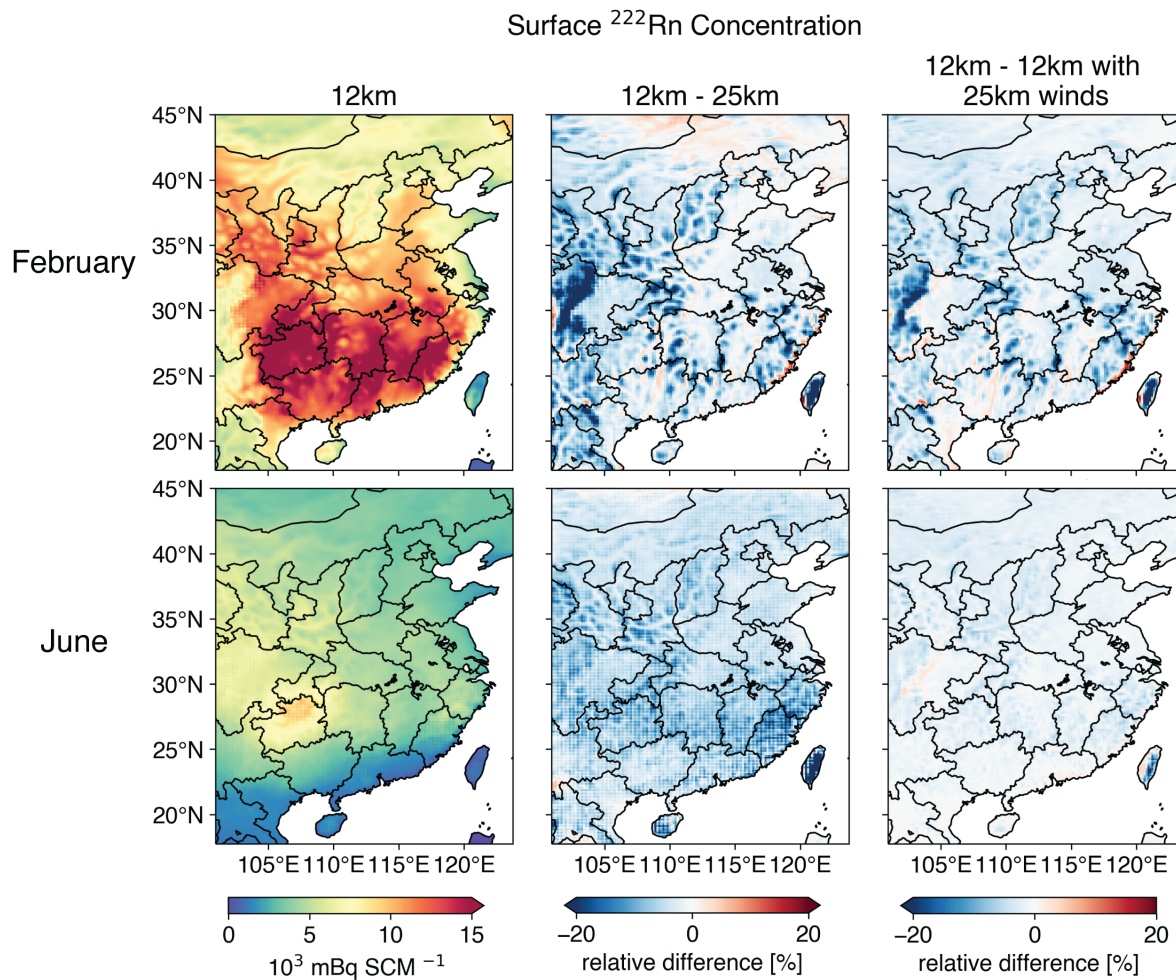
453 Zhang, B., Liu, H., Crawford, J. H., Chen, G., Fairlie, T. D., Chambers, S., Kang, C.-H.,
454 Williams, A. G., Zhang, K., Considine, D. B., Sulprizio, M. P., and Yantosca, R. M.: Simulation
455 of radon-222 with the GEOS-Chem global model: emissions, seasonality, and convective
456 transport, *Atmospheric Chem. Phys.*, 21, 1861–1887, <https://doi.org/10.5194/acp-21-1861-2021>,
457 2021.

458 Zhang, L., Liu, L., Zhao, Y., Gong, S., Zhang, X., Henze, D. K., Capps, S. L., Fu, T.-M., Zhang,
459 Q., and Wang, Y.: Source attribution of particulate matter pollution over North China with the
460 adjoint method, *Environ. Res. Lett.*, 10, 084011, <https://doi.org/10.1088/1748-9326/10/8/084011>,
461 2015.

462 Zheng, B., Tong, D., Li, M., Liu, F., Hong, C., Geng, G., Li, H., Li, X., Peng, L., Qi, J., Yan, L.,
463 Zhang, Y., Zhao, H., Zheng, Y., He, K., and Zhang, Q.: Trends in China’s anthropogenic
464 emissions since 2010 as the consequence of clean air actions, *Atmospheric Chem. Phys.*, 18,
465 14095–14111, <https://doi.org/10.5194/acp-18-14095-2018>, 2018.

466 Zhuang, J., Jacob, D. J., Gaya, J. F., Yantosca, R. M., Lundgren, E. W., Sulprizio, M. P., and
467 Eastham, S. D.: Enabling Immediate Access to Earth Science Models through Cloud Computing:
468 Application to the GEOS-Chem Model, *Bull. Am. Meteorol. Soc.*, 100, 1943–1960,
469 <https://doi.org/10.1175/BAMS-D-18-0243.1>, 2019.

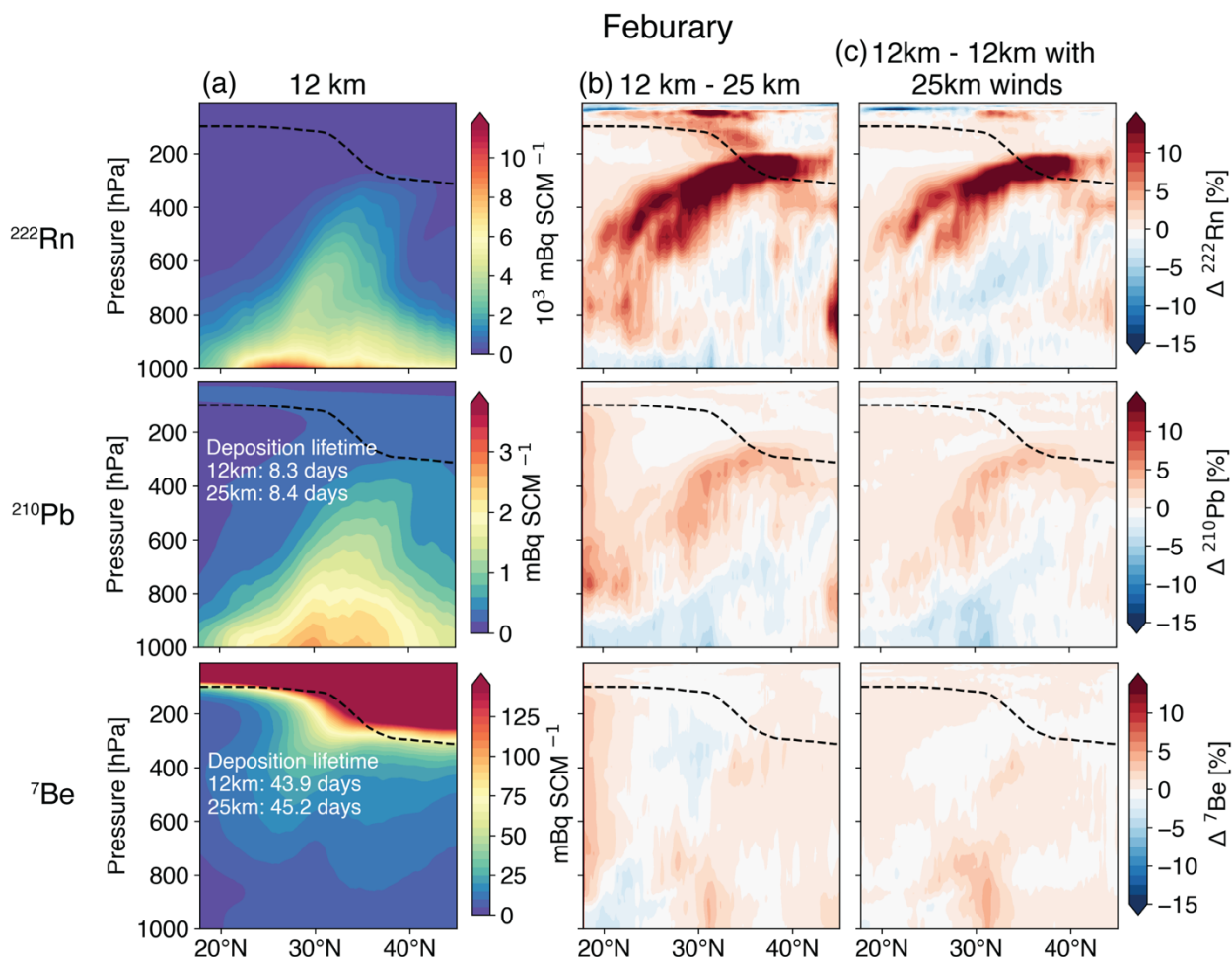
470



472 **Figure 1.** Monthly mean surface ^{222}Rn mixing ratios (mBq SCM^{-1}) simulated over eastern China
 473 in February and June 2022. Columns from left to right show the concentrations simulated by
 474 GEOS-Chem at 12-km resolution, the relative differences with a simulation at 25-km resolution,
 475 and the relative differences between two 12-km simulations driven by the 12-km and 25-km
 476 GEOS-FP advection archives, respectively. SCM is a standard cubic meter of air at 0 °C (273.15
 477 K) and 1 atm (1013.25 hPa).

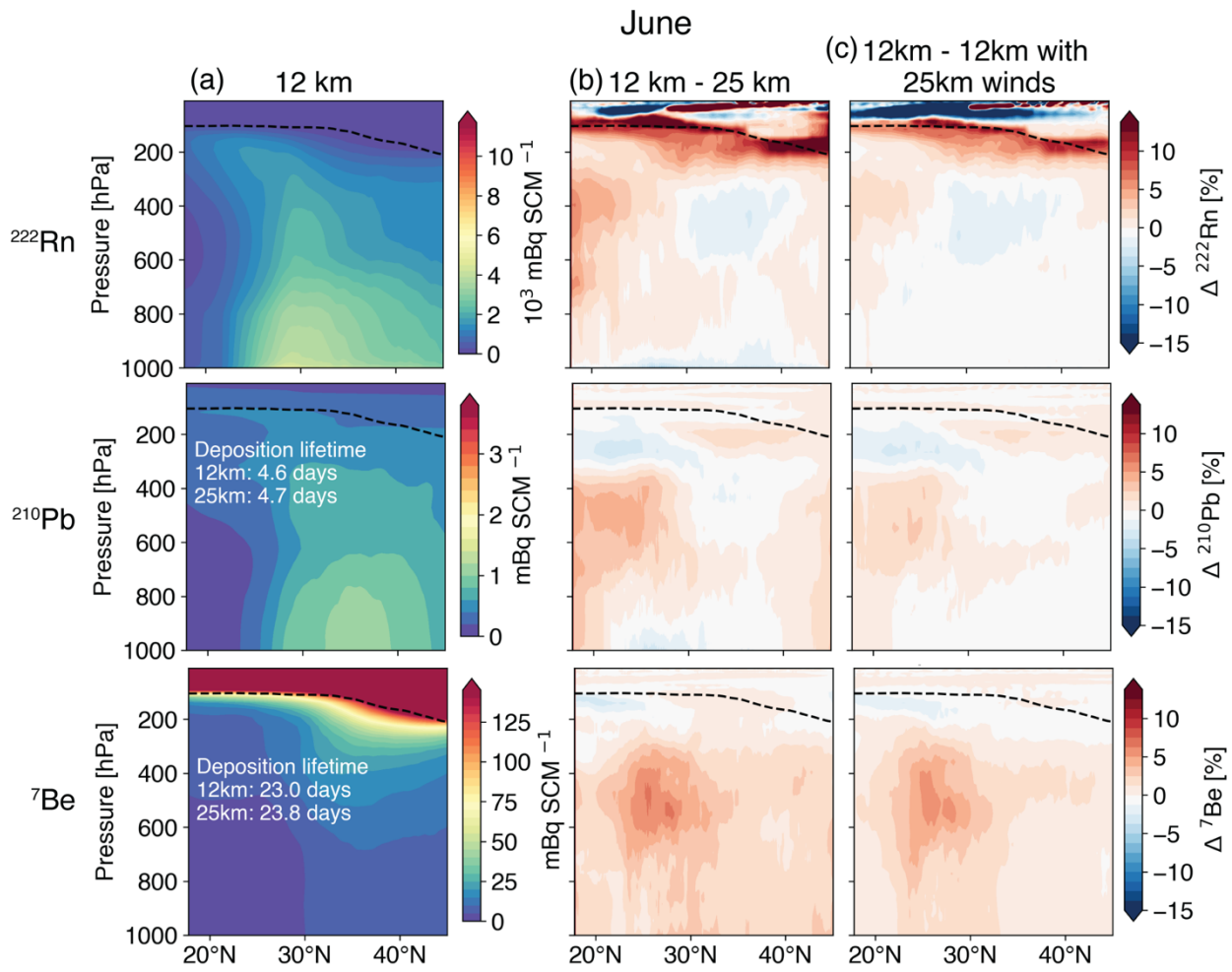
478

479



481 **Figure 2.** Zonally averaged latitude-pressure monthly mean mixing ratios of ^{222}Rn , ^{210}Pb , and
 482 ^{7}Be simulated by GEOS-Chem for February 2022 over the eastern China domain of Figure 1 at
 483 12-km resolution (left column), the relative differences with a 25-km simulation (middle column)
 484 and relative differences with a 12-km simulation driven by the 25-km advection archive (right
 485 column) Lifetimes of tropospheric ^{210}Pb and ^{7}Be against deposition are inset. The dashed black
 486 lines indicate the tropopause.

487



488 **Figure 3.** Same as Figure 2 but for June 2022.

489

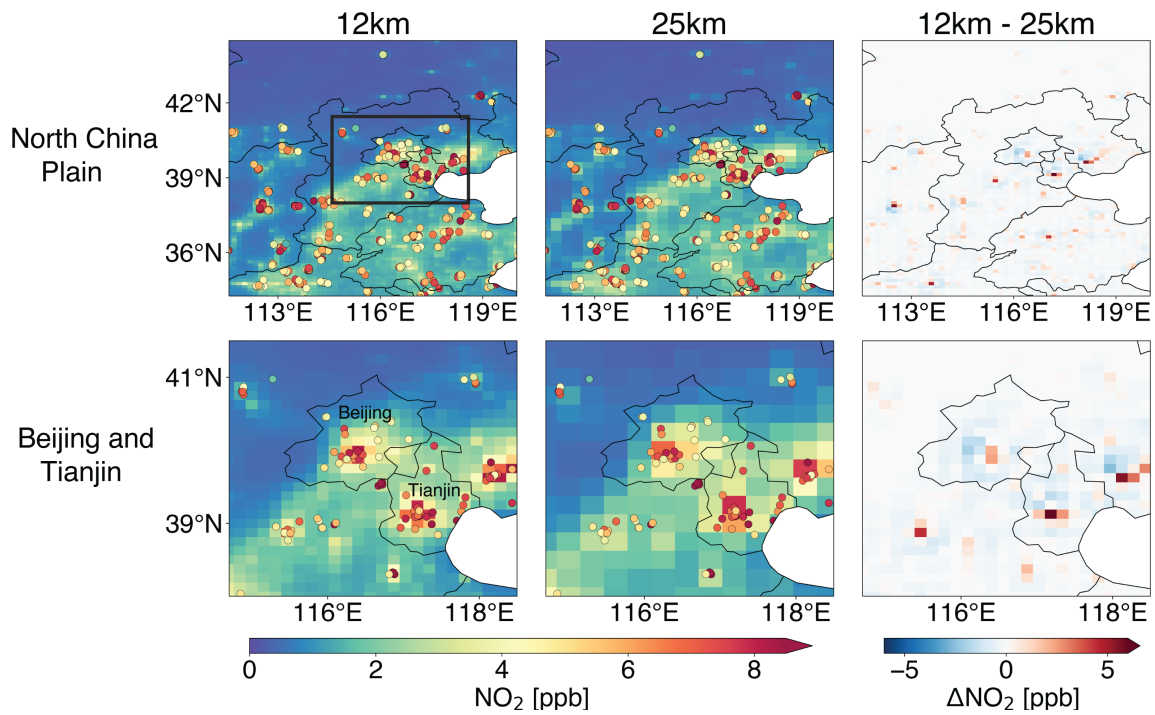
490

491

492

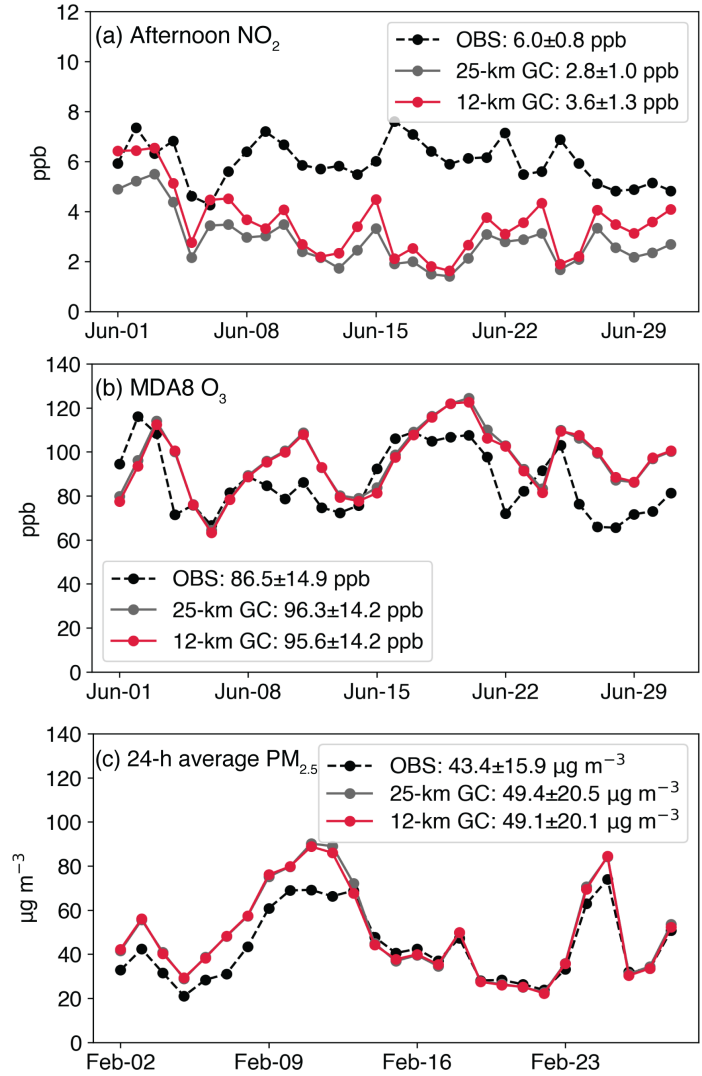
493

494



495 **Figure 4.** Afternoon (13–18 local time) monthly mean surface NO₂ concentrations in June 2022
496 simulated by GEOS-Chem at 12-km and 25-km resolution, for the North China Plain (NCP) and
497 for Beijing and Tianjin (box in top left panel). Circles show CNEMC network observations.

498



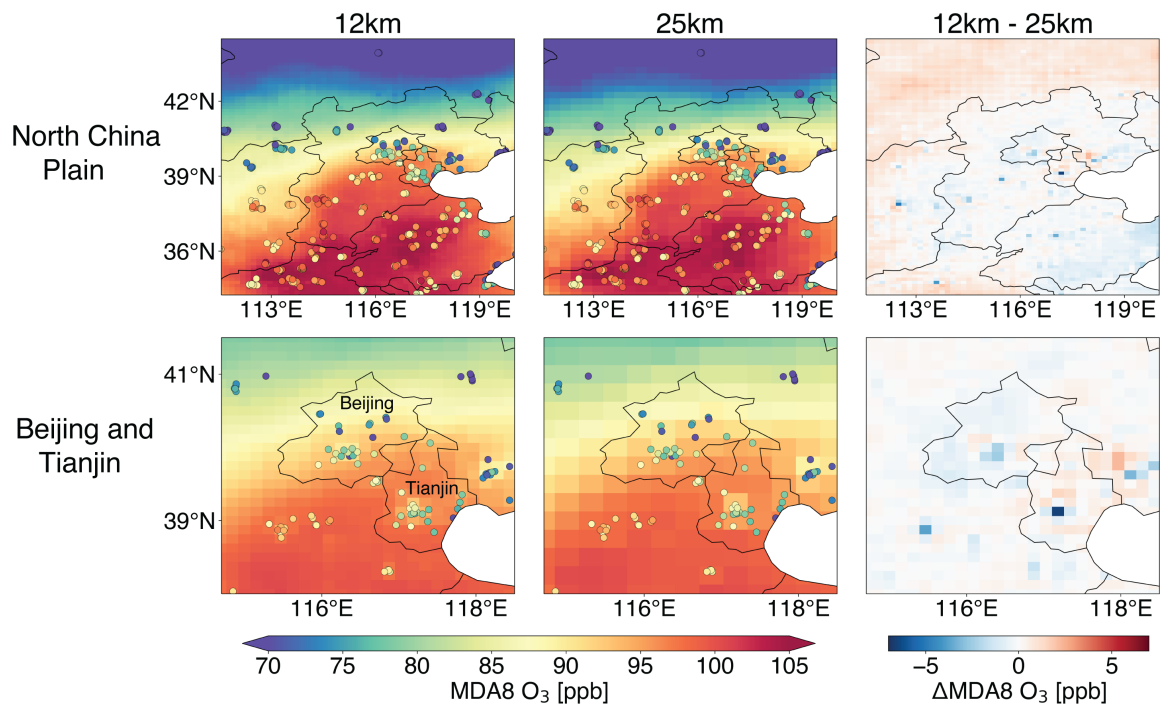
499

500

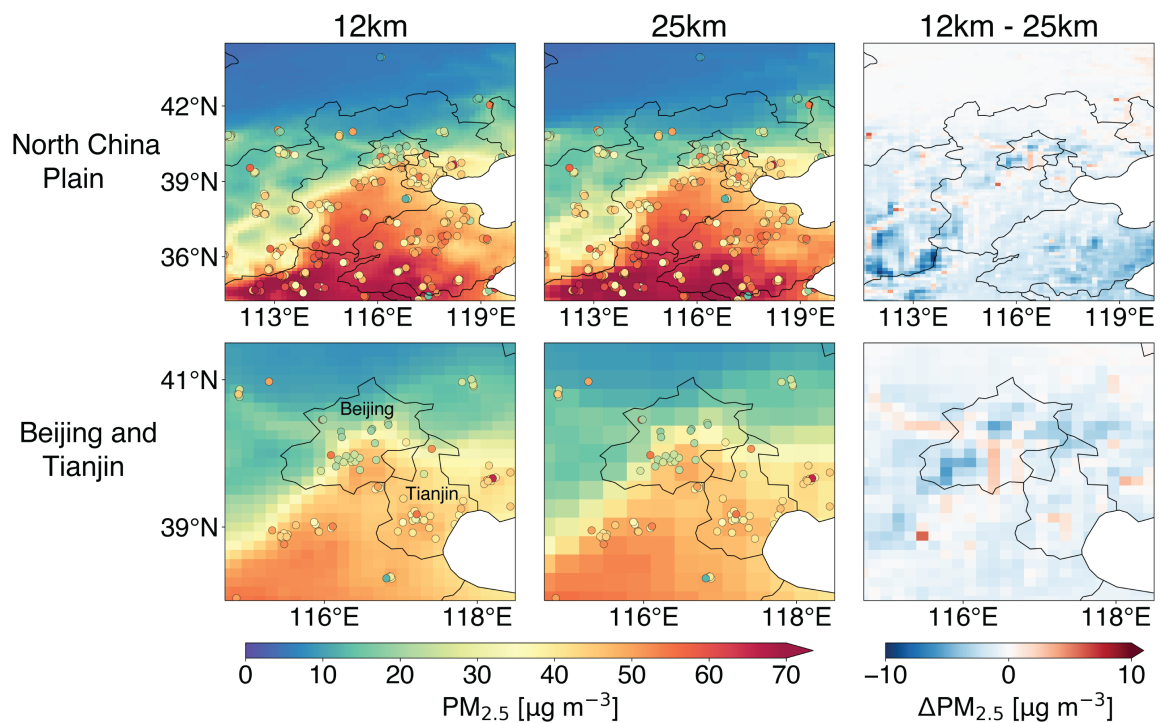
501 **Figure 5.** Daily time series of surface concentrations in the North China Plain (NCP): (a)
 502 afternoon (13–18 local time) NO_2 in June 2022, (b) maximum daily 8-h average (MDA8) ozone
 503 in June 2022, and (c) 24-h average $\text{PM}_{2.5}$ in February 2022. Observations at China National
 504 Environmental Monitoring Center (CNEMC) sites, shown as circles in Figure 4 and averaged
 505 over the NCP domain, are compared to GEOS-Chem simulations at 12- and 25-km resolution for
 506 the same sites. Monthly mean values and standard deviations across all domain sites are shown
 507 inset.

508

509



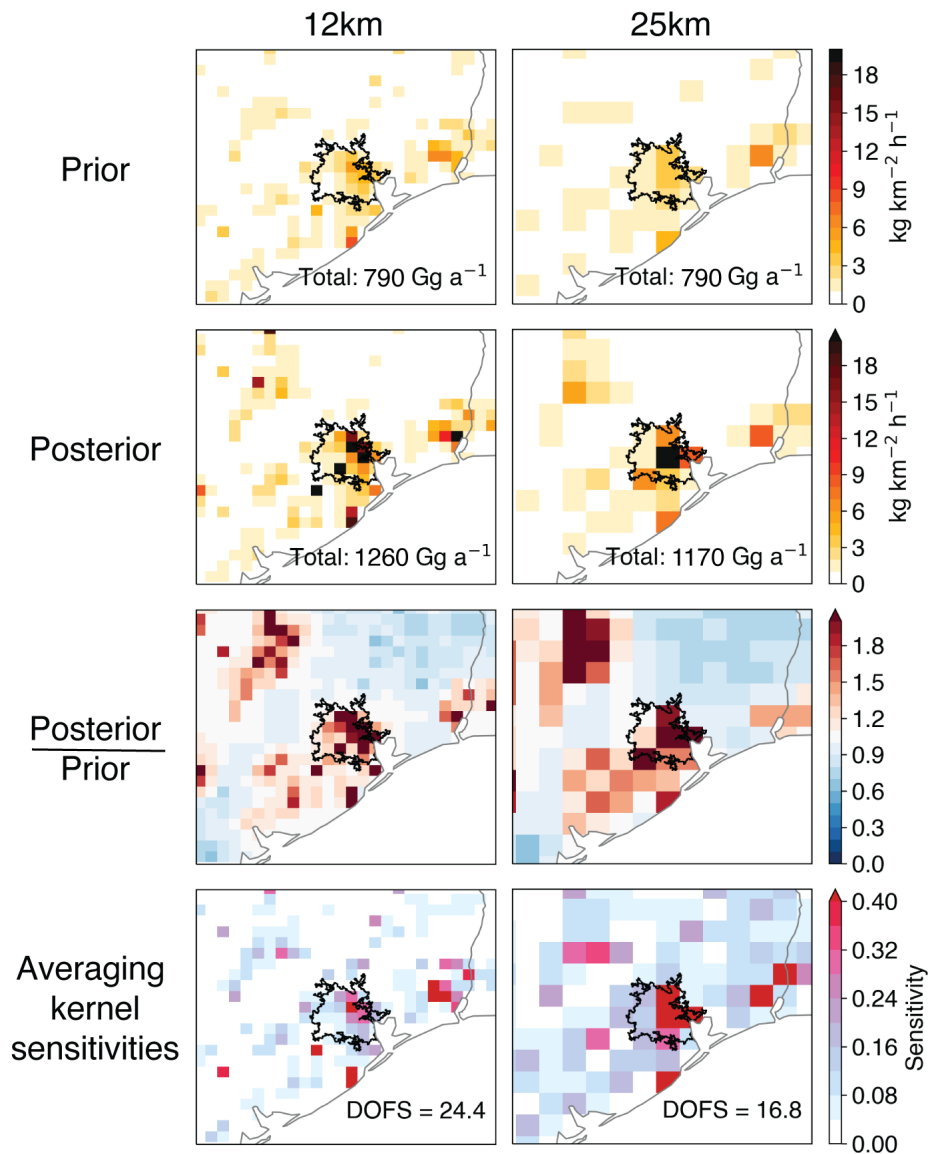
510 **Figure 6.** Same as Figure 4 but for surface MDA8 ozone concentrations in June 2022.



511
512 **Figure 7.** Same as Figure 4 but for surface 24-h average PM_{2.5} concentrations in February 2022.

513

514



515

516 **Figure 8.** Methane emissions in the Houston area of eastern Texas ($3^{\circ}\times 4^{\circ}$ domain) inferred from
 517 TROPOMI satellite observations using the Integrated Methane Inversion (IMI) at 12- and 25-km
 518 resolution. Panels from top to bottom are prior emissions from bottom-up inventories; posterior
 519 emissions from the inversion; ratio of posterior to prior emissions; and averaging kernel
 520 sensitivities that quantify the sensitivity of the posterior estimates to the true state. The Houston
 521 urban boundary (US Census Bureau, 2017) is delineated in black. Emission totals over the whole
 522 $3^{\circ}\times 4^{\circ}$ domain are shown inset in the top two rows. The sum of area-weighted averaging kernel
 523 sensitivities for the whole domain defines the Degrees of Freedom for Signal (DOFS) inset in the
 524 bottom panels.